






RESEARCH ARTICLE

10.1029/2021JA030121

Simultaneous Detection of Signatures of Conjugate Photoelectrons in the Ionosphere and Thermosphere

Hyosub Kil¹ , Larry J. Paxton¹ , and Robert K. Schaefer¹ 

¹The Johns Hopkins University Applied Physics Laboratory, Laurel, MD, USA

Key Points:

- Enhancements in ion temperature, ion density, and far ultraviolet emission are observed at night in the winter (dark) hemisphere
- Morphology of these phenomena agrees with the predicted morphology of conjugate photoelectron (CPE) flow from the sunlit side
- Increase in the oxygen ion density scale height by CPE heating elevates oxygen ion density, oxygen ion fraction, and total ion density

Correspondence to:

H. Kil,
hyosub.kil@jhuapl.edu

Citation:

Kil, H., Paxton, L. J., & Schaefer, R. K. (2022). Simultaneous detection of signatures of conjugate photoelectrons in the ionosphere and thermosphere. *Journal of Geophysical Research: Space Physics*, 127, e2021JA030121. <https://doi.org/10.1029/2021JA030121>

Received 10 NOV 2021
Accepted 11 MAY 2022

Author Contributions:

Conceptualization: Hyosub Kil, Larry J. Paxton, Robert K. Schaefer
Formal analysis: Hyosub Kil
Funding acquisition: Larry J. Paxton
Investigation: Hyosub Kil
Methodology: Hyosub Kil
Project Administration: Hyosub Kil, Larry J. Paxton
Software: Hyosub Kil
Supervision: Hyosub Kil
Validation: Hyosub Kil, Larry J. Paxton, Robert K. Schaefer
Visualization: Hyosub Kil
Writing – original draft: Hyosub Kil
Writing – review & editing: Hyosub Kil, Larry J. Paxton, Robert K. Schaefer

© 2022. The Authors.

This is an open access article under the terms of the [Creative Commons Attribution-NonCommercial-NoDerivs License](https://creativecommons.org/licenses/by/4.0/), which permits use and distribution in any medium, provided the original work is properly cited, the use is non-commercial and no modifications or adaptations are made.

Abstract We investigate the impact of conjugate photoelectrons (CPEs) on the topside (~600 km altitude) ionosphere at low and midlatitudes using measurements of the ion temperature, density, and composition from the first Republic of China satellite during a period of the high to moderate solar activity (March 1999 to June 2004). Elevated ion temperatures and densities are observed in the dark Northern American-Atlantic sector during the December solstice and in the Australian sector during the June solstice. The oxygen ion fraction and density are also elevated at these locations. These observations indicate that photoelectrons from the conjugate hemisphere heat the local ionospheric plasma. The morphology of the ion temperature in the winter hemisphere is well represented by the solar zenith angle in the sunlit conjugate hemisphere. The CPE hypothesis for the observed ionospheric heating is confirmed by coincident nighttime enhancements of the far ultraviolet airglow measured by the Global Ultraviolet Imager onboard the Thermosphere Ionosphere Mesosphere Energetics and Dynamics satellite.

1. Introduction

Solar extreme ultraviolet photons have energy in excess of the ionization energy of thermospheric constituents (O, N₂, and O₂) and produce photoelectrons with energies much greater than the ambient electron energy. Most of the excess photon energy go to the photoelectron kinetic energy because of the large difference between the electron and ion masses. The intense 30.4 nm solar irradiance produces prominent peaks in the photoelectron spectrum ranging from ~22 to ~27 eV. These suprathermal photoelectrons lose energy primarily through inelastic collisions with the ambient neutral particles below about 350 km. Once their energy is reduced below about 5 eV, they lose much of their remaining energy to the thermal electrons, finally becoming part of the thermal electron populations. The thermal electrons lose their energy via Coulomb collisions with the ambient ions and in inelastic collisions with ambient neutrals (Schunk & Nagy, 1978). The heated ambient ions are cooled by collisions with the ambient neutrals. The excess neutral heat energy is rapidly conducted to much lower altitudes.

At high altitudes (above ~300 km), where the mean free path of photoelectrons is greater than the atmospheric scale height, photoelectrons can escape from the local ionosphere and travel to the opposite hemisphere along geomagnetic field lines (Hanson, 1963; Nagy & Banks, 1970; Richards & Peterson, 2008; Schunk & Nagy, 1978; Urco et al., 2021). The photoelectrons from the sunlit conjugate hemisphere result in ionization and heating of the neutrals and electrons in the dark hemisphere. They also excite airglow. The conjugate photoelectrons (CPEs) heat thermal electrons as they pass through the plasmasphere. This heat is conducted down into both hemispheres and results in elevated electron temperatures in the topside where the thermal electron cooling rate is low. Some of the topside thermal electron energy is transferred to the local ions by Coulomb collisions. Because ion heat conduction is small and the neutral densities are low in the topside, this electron-ion heat transfer results in elevated ion temperatures in the topside ionosphere. The thermal electron temperature is still elevated at lower altitudes, but there the ion temperature is only slightly elevated above the neutral temperature because the ions are rapidly cooled by collisions with neutrals.

The signatures of CPEs have been identified by the observations of anomalous enhancements in the electron and ion temperatures, electron density, airglow, and photoelectron flux (Bennett, 1969; Buckley & Moos, 1971; H. C. Carlson, 1966; R. W. Carlson & Suzuki, 1974; Chao et al., 2003; Christensen, 1975; Evans, 1967; Evans & Gastman, 1970; Kakinami et al., 2010; Kil et al., 2020; Meier, 1971; Oyama et al., 1996; Shepherd et al., 2014; Solomon et al., 2020; Yang et al., 2020). Most of these studies focused on event-based case studies using observations during limited periods. A few studies reported the global morphology of CPEs. Chao et al. (2003) derived the pre dawn morphology of CPEs using the measurements of the ion temperature by the first Republic of China

satellite (ROCSAT-1). Recently, Kil et al. (2020) derived the global morphology of predawn CPEs using the measurements of the oxygen atom (OI) 130.4 nm emission by the Special Sensor Ultraviolet Spectrographic Imager (Paxton et al., 1993) onboard the Defense Meteorological Satellite Program F18 satellite. Solomon et al. (2020) identified the distribution of CPEs in the premidnight and postmidnight in the American-Atlantic sector using the measurements of the OI 135.6 nm emission by the Global-scale Observations of the Limb and Disk (GOLD) satellite. These studies provide some global-scale information on CPEs, but there still exists a gap. Chao et al. (2003) and Kil et al. (2020) only reported the ionospheric and thermospheric signatures of CPEs at predawn. Solomon et al. (2020) reported the signatures of CPEs at both premidnight and postmidnight, but the GOLD observations were available only in the American-Atlantic sector. Thus, the premidnight global morphology of CPEs has not yet been reported.

The electron temperatures in the equatorial region and midlatitudes are controlled by different processes due to the difference in the magnetic field geometry (the L-shell that the sample latitude is on). At midlatitudes, the heat conduction along magnetic field lines from the plasmasphere controls the electron temperature in the topside *F* region (Evans, 1973; Schunk & Nagy, 1978). The thermal electrons in the topside can maintain higher temperatures than the ion and neutral gas temperatures at night due to the heat conduction from above. The ion temperature in the topside is also controlled by the electron heat conduction because ions are heated by electrons. At low latitudes, the heat capacity is small because the flux tube volume is small, and the heat conduction from the plasmasphere is inhibited because of the near-horizontal magnetic field lines.

In the ionosphere, electrons lose energy to ions and ions lose energy to neutrals by collisions. Because these processes occur faster for higher electron and ion densities, both the electron and ion temperatures are sensitive to the ion density. The anticorrelation between the electron/ion temperature and plasma density demonstrates the significant role of the plasma density in the electron/ion temperature (e.g., Kakinami et al., 2014; Yang et al., 2020). Thus, accurate knowledge of the plasma density is essential for the clarification of the signatures of CPEs in the electron/ion temperature. The nighttime enhancement of the topside ion temperature in a localized region can be attributed to the low plasma density in the presence of a plasmasphere heat flow that may be caused by CPEs. Chao et al. (2003) interpreted the ion temperature enhancement at night in terms of the effect of CPEs, but that study did not provide a comparison of the ion temperature and density.

This report investigates the CPE heating of the ionosphere and associated changes in the plasma density and ion composition. The CPE signatures in the ionosphere are identified from the measurements of the ion temperature, density, and composition from March 1999 to June 2004 by the ROCSAT-1. Confirmation of the link between CPEs and the elevated ion temperatures is provided by airglow measurements from the Global Ultraviolet Imager (GUVI) experiment on the Thermosphere Ionosphere Mesosphere Energetics and Dynamics (TIMED) satellite (Paxton et al., 1999, 2004, 2017).

2. Data Description

ROCSAT-1 (renamed as Formosat-1 in December 2004) was the first experimental scientific satellite of National Space Program Office (now the National Space Organization) of Taiwan. The science objectives of the mission were to perform ocean color imaging, investigate plasma electrodynamics in the ionosphere, and enable telecommunication. ROCSAT-1 was launched on 27 January 1999 near solar maximum (F10.7–180) and its measurement campaign ended during medium solar activity (F10.7–100) on 17 June 2004. The orbital inclination was 35°, altitude was ~600 km, and orbital period was 97 min. The Plasma and Electrodynamics Instrument provided measurements of the ion density, composition, velocity, and temperature (Su et al., 2001). This study uses the measurements of the ion density, composition, and temperature from March 1999 to June 2004. The data sampling cadence for both the ion density and temperature is 1 s.

The measurements of the ion density by ROCSAT-1 have been extensively used for the study of the electrodynamics and irregularities at low and midlatitudes, but the measurements of the ion temperature have had limited use. The raw ion temperature data have many values that deviate greatly from the mean temperature due to various factors, including electronic noise, nonuniform electrical potential distribution across the grid surfaces in the instrument, non-Maxwellian distribution of space plasma, and errors in the current-voltage curve fitting. The Savitzky-Golay filter (Savitzky & Golay, 1964) is used to remove those outliers. Figure 1 shows an example of the

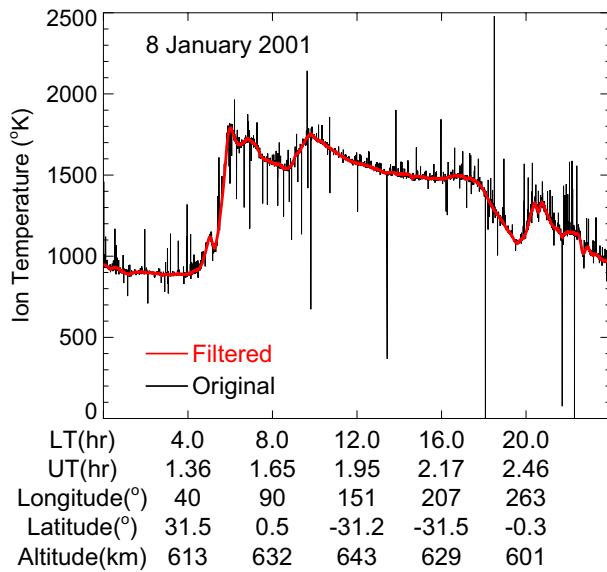


Figure 1. A sample observation of the ion temperature measured by ROCSAT-1. The raw data and the result after a low-pass-filter that has been applied are shown by the black and red curves, respectively.

ion temperature measurements (thin black line) and the filtered data (thick red line). The ion density measurements do not require filtering.

TIMED was the first mission of the Solar Terrestrial Probes program from the National Aeronautics and Space Administration in the United States. The goal of the mission was to understand the energy transfer into and out of the mesosphere, lower thermosphere, and ionosphere. TIMED was launched on 7 December 2001 and is still in operation. The orbital inclination is 74° and the altitude is 630 km. GUVI, one of the four instruments on TIMED, obtains the FUV spectrum (Christensen et al., 2003; Paxton et al., 2004, 2017, 2021). In an “imaging mode”, GUVI provides imaging data at five FUV wavelength intervals or colors (121.6, 130.4, 135.6, 140–150, and 165–180 nm). Since about 2008, GUVI has telemetered back the entire spectrum in a “spectrograph” mode. Currently, GUVI provides only spectrograph data at a fixed disk look angle due to the failure of the scan mirror mechanism. The radiative recombination of oxygen ion (O^+) ions with thermal electrons in the ionosphere produces both the 130.4 and 135.6 nm emissions. The 130.4 and 135.6 nm intensity ratios associated with radiative recombination are approximately 1.2 (Strickland & Anderson, 1977; Zhang et al., 2021). In the region where CPEs are likely, the 130.4 nm intensity is several times greater than the 135.6 nm intensity, providing evidence that the 130.4 nm airglow is created by CPEs rather than by radiative recombination. In this study, the maps of 130.4 nm emission using the GUVI level 1B (calibrated and geolocated) disk-scan data on 4 days during solstices are presented.

3. Observational Results and Discussion

Section 3.1 gives an overview of the CPE signatures in the ionosphere using the ROCSAT-1 observations on 27 December 2003 and examines the effect of the ion density on the ion temperature by comparing their morphologies. Section 3.2 investigates the mean behavior of the ionospheric CPE signatures using maps of the ion temperature, density, and O^+ fraction during solstices using data from March 1999 to June 2004. Because the morphologies of the ionospheric parameters do not vary much during this period, the maps were produced using all data. The CPE origin of the temperature signatures is assessed by comparing the morphologies of the ionospheric parameters with the solar zenith angle (SZA) in the sunlit conjugate hemisphere. The CPE signatures in the thermosphere are investigated in Section 3.3 using the TIMED/GUVI data.

The interpretation of CPE signatures in the temperature and ion density data is not straightforward because many factors, such as neutral winds, neutral composition, magnetic declination, and magnetic inclination, can affect the morphology of the plasma density at night (Burns et al., 2008, 2011; C. H. Chen et al., 2011; Y. Chen et al., 2016; He et al., 2009; Horvath, 2006; Horvath & Essex, 2003; Jee et al., 2009; Kil et al., 2006; Klimenko et al., 2015; Lee et al., 2018; Lin et al., 2009, 2010; Liu et al., 2011; Lomidze et al., 2016; Richards et al., 2017, 2018; Sultan & Rich, 2001; West & Heelis, 1996; West et al., 1997). In addition, the plasma temperature is sensitive to the plasma density. We assess ionospheric CPE signatures using the SZA morphology in the sunlit conjugate hemisphere, but a self-consistent numerical simulation would be required to fully explore the effects of other factors on the ion temperature and density. That is beyond the scope of this report.

3.1. Overview of ROCSAT-1 Observations

Figure 2 shows measurements of (a) the ion temperature and (b) the total ion density (black) and O^+ fraction (red) along seven ROCSAT-1 orbits as a function of the universal time for 27 December 2003. Figure 2c shows the SZA along the ROCSAT-1 orbit (dotted black line) and its magnetic conjugate location (thick red line). Figure 2d shows the longitude (thin black line) and latitude (thick red line) along the ROCSAT-1 orbits. The vertical blue-dotted and red-dashed lines indicate 04 and 08 local times (LT), respectively, which are based on the longitude at the location of the equator crossing of the satellite. On each day, there are ion temperature spikes (pronounced spikes are labeled by “B”) just before 08 LT corresponding to local sunrise, followed by a

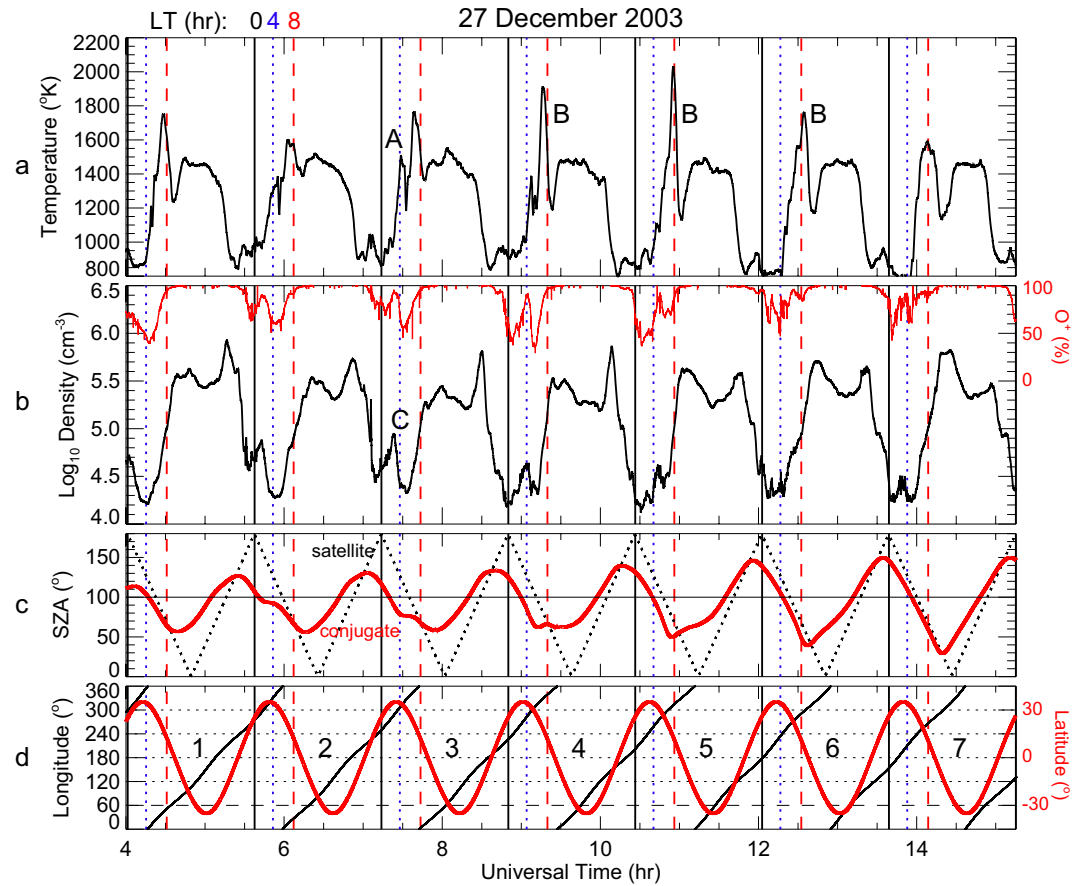


Figure 2. Orbital and diurnal variation of the (a) ion temperature, (b) ion density (black) and O^+ (red) fraction, (c) solar zenith angles (SZAs) at the ROCSAT-1 orbit (black) and its conjugate location (red thick), and (d) latitude (black dotted) and longitude (red thick) for 7 ROCSAT-1 orbits on 27 December 2003. The vertical black solid, blue dotted, and red dashed lines indicate 00:00 hr, 04:00, and 08:00 LT, respectively. The satellite altitude is ~ 600 km. The labels “A”, “B”, and “C” indicate nighttime temperature increase, morning overshoot, and nighttime density increase, respectively. The locations of their peaks are indicated in Figures 4 and 7.

rapid decay. The temperature spike is most pronounced when the satellite is near 300°E longitude and 15°N latitude. For these low-latitude spikes, the Field Line Interhemispheric Plasma (FLIP) model (Richards & Wilkinson, 1998; Richards et al., 1998) calculations indicate that conjugate sunrise occurred 3–4 hr prior to the satellite passage, and both ends of the field line had been fully illuminated for 1.5–2 hr. The temperature minima after 08 LT occur when the satellite is over the equator where the ion density is high and the O^+ density approaches 100%. The smaller temperature spikes (labeled “A”) near 04 LT on days 2, 3, and 4 correspond to the time of conjugate sunrise. These spikes occur when the satellite is in the North American sector near 300°E longitude and 30°N latitude. In the evening, after sunset in both hemispheres, the temperatures and densities are low because the satellite is located on magnetic flux tubes that have limited heat capacity.

The temperature spike around 08 LT is referred to as the “morning overshoot” in the electron temperature (Evans, 1965; Farley et al., 1967; Otsuka et al., 1998; Oyama et al., 1996; Stolle et al., 2011; Yang et al., 2020). The electron temperature overshoot in the morning is produced by the prompt heating of the ambient thermal electrons by photoelectrons produced by the onset of the local sunrise beginning at high altitudes. As the SZA decreases, ions and electrons are increasingly produced at lower altitudes. This results in a sharp increase in the electron cooling rate, which is quadratic in electron/ion density. Since the thermal electron heating is linear in electron density, the enhanced electron-ion cooling causes a rapid drop in electron temperature. Because thermal electrons are the heating source of the ions, the morning overshoot also appears in the ion temperature. As we show later (Figure 7), the intensity of the morning overshoot depends on the magnetic declination.

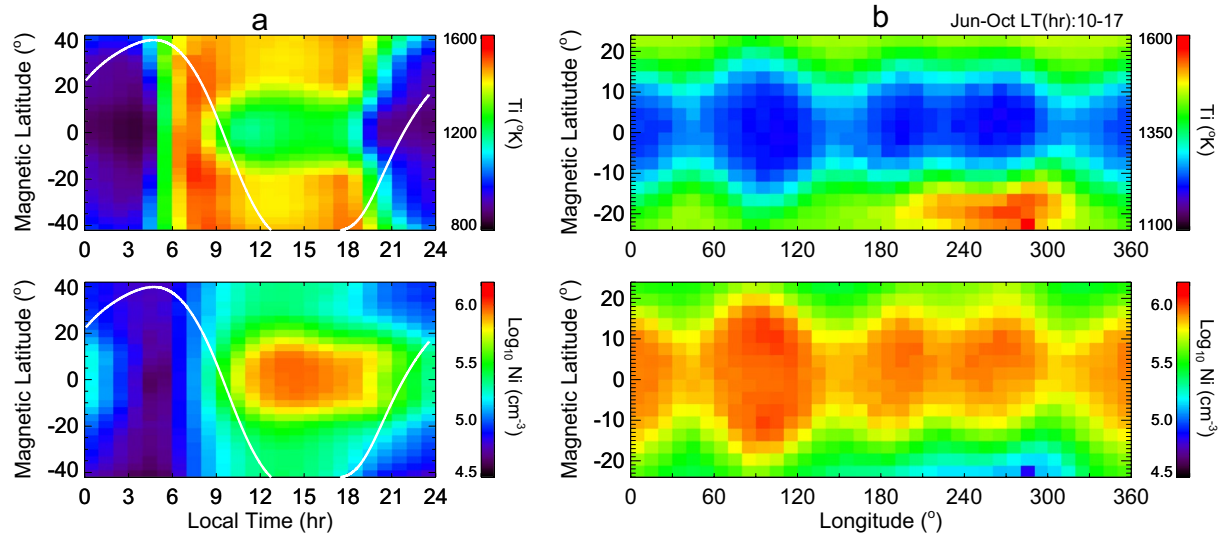


Figure 3. (a) Distributions of the ion temperature and density in the LT and magnetic latitude coordinates from ROCSAT observations in March 1999 to June 2004. The white line is the ROCSAT-1 orbit 6 in Figure 2. (b) Distributions of the ion temperature and density in the longitude and magnetic latitude coordinate from ROCSAT observations at 10:00–17:00 LT in June–October.

Of primary interest to the current investigation are the small temperature peaks near 04 LT on orbits 2, 3, and 4 in Figure 2. One of them is labeled “A” in orbit 3. They are interpreted as arrival signals of photoelectrons from the conjugate hemisphere while the local hemisphere is still dark. These increases are observed between 300° and 320°E longitude (North American sector) and ~30°N latitude when the conjugate SZA is less than 100°. These signatures are not seen on the other orbits because the conjugate SZA was 100° or more. Orbits 2–4 are also distinguished from other orbits by the development of pronounced localized density increases between midnight and 04:00 LT. One of them is labeled “C”. The detection times and locations of the localized density increases are slightly earlier than those of the localized temperature increases. The nighttime increases in the *F* region peak plasma density at midlatitudes, especially in winter, are a well-known phenomenon (Evans, 1965; Mikhailov & Förster, 1999; Mikhailov et al., 2000; Pavlov & Pavlova, 2005; Richards, Buonsanto, et al., 2000), but its generation mechanism is not understood. The O⁺ fraction decreases to as little as ~50% at night, but it reaches ~90% as the localized nighttime density increases.

The inverse relationship between density and temperature can provide a diagnostic for identifying the CPE signatures in the ionosphere. Figure 3 displays the inverse relationship of the ion density and temperature as a function of LT, longitude, and magnetic latitude. Because this plot uses magnetic latitude, the higher latitudes are weighted to the American longitudes in the North and the 0°–180°E longitude range in the South. The LT variations of ion temperature and density with latitude are shown in the left two panels (Figure 3a). The white lines indicate the satellite path 6 shown in Figure 2. The diurnal temperature and density variations along the satellite paths in Figure 2 can be understood in conjunction with the mean behavior shown in Figure 3a. The temperature is high at all latitudes between 06:00 and 09:00 LT while the density is low. As the SZA decreases, the density increases, and the temperature decreases. A notable feature is the formation of a temperature hole in the equatorial region during daytime. The morphology of the temperature hole matches the morphology of the ion concentration. Thus, the anticorrelated relationship between the ion density and temperature dominates the latitudinal behavior of the ion temperature. The morphology of the ion temperature shown in Figure 3a agrees with the morphology of the electron temperature found by Yang et al. (2020).

The right two plots (Figure 3b) map the ion temperature and density using the 10:00–17:00 LT data for June–October. This period was selected because the wave number 4 structure in the plasma density is known to be pronounced during daytime in these months (Kil & Paxton, 2011). Figure 3b shows the formation of anticorrelated wave number 4 patterns in the ion temperature and density. The high ion temperature at 180°–330°E longitude in the Southern Hemisphere also agrees with the low ion density in that region. The observations shown in Figure 3 indicate that the topside ion temperature can be used as a tracer of the ion density morphology (or vice versa) on the dayside at low latitudes. The longitudinal wave number 4 structure is a prominent feature in the ion

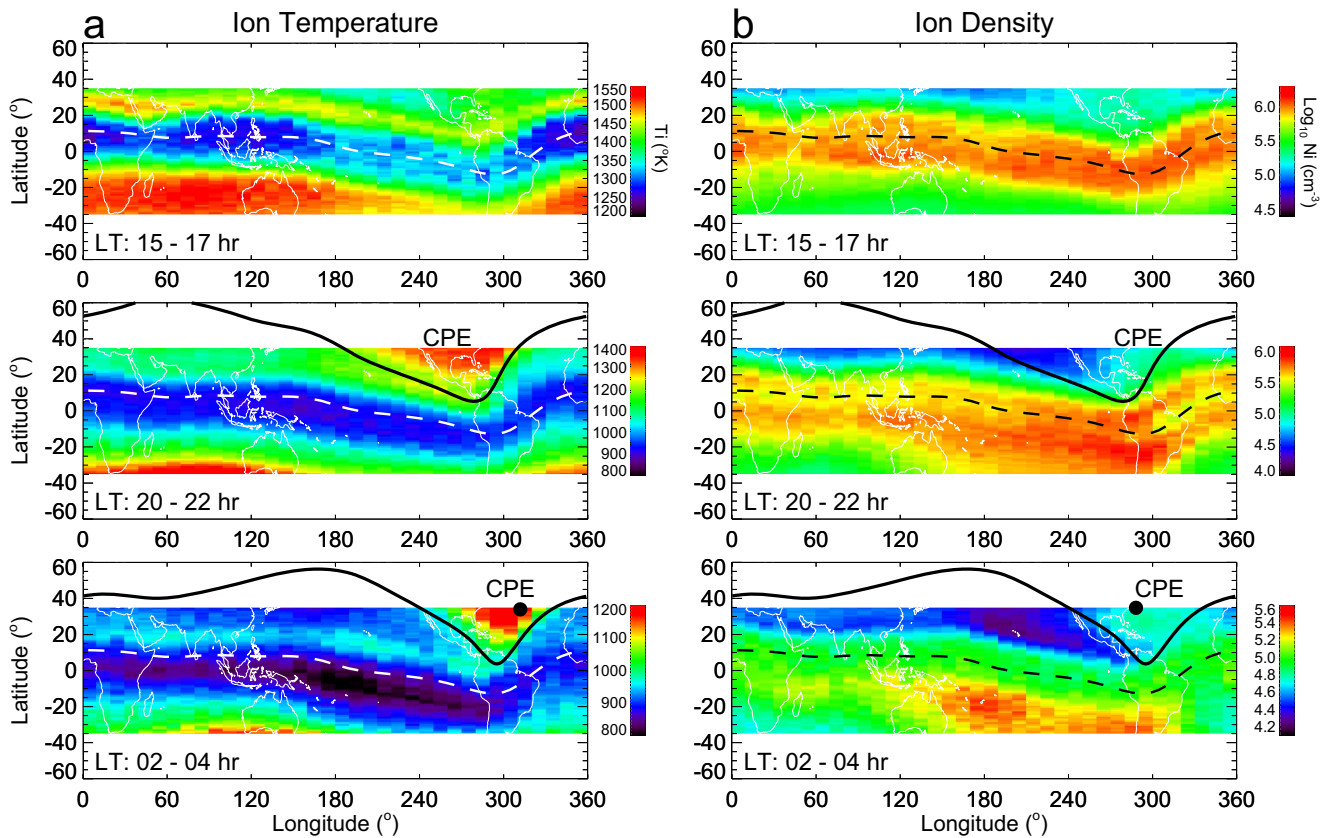


Figure 4. Comparison of the morphologies of the (a) ion temperature and (b) ion density at three LT (15:00–17:00, 20:00–22:00, and 02:00–04:00) around the December solstice (November, December, January, and February). The black solid lines are the predicted equatorward boundaries of conjugate photoelectrons (CPEs) at 20:00 and 04:00 LT. The anticorrelation between ion density and temperature is observed except for the region where photoelectrons from the sunlit area are propagating to a nightside conjugate region. The locations of CPEs are indicated in the figures. Black dots correspond to the locations of the localized temperature and density peaks indicated by labels “A” and “C” in Figure 2.

density and vertical ion velocity and has been attributed to the modulation of the E region dynamo by nonmigrating atmospheric tides (England et al., 2006; Immel et al., 2006; Kil & Paxton, 2011; Kil et al., 2007, 2008; Lin et al., 2007; Sagawa et al., 2005; Scherliess et al., 2008).

3.2. Conjugate Photoelectron Signatures in the Ionosphere—Statistical Results

The anticorrelation between the ion temperature and density persists in the night, but deviations from anticorrelation emerge at night. Because the deviations are pronounced in winter during solstices, our investigation focuses on the observations around the December solstice (November–January) and the June solstice (May–July). Figure 4 shows the distributions of (a) the ion temperature (left panels) and (b) the ion density (right panels) around the December solstice for three LTs: 15:00–17:00 (top), 20:00–22:00 (middle), and 02:00–04:00 (bottom). The solid black lines are the predicted equatorward boundaries of CPEs at 20 and 04 LT based on a SZA of 100° at the magnetic conjugate locations in the summer hemisphere (Kil et al., 2020). The boundary of CPEs varies with LT and the day of the year. Here, the boundaries are calculated for 20:00 and 04:00 LT at the geographic equator on 15 December. Because the maps of the ion temperature and density are produced using the data for a 3-month period and because the LT along a magnetic field line varies with latitude, there exists a certain range of variation in the boundary from the black lines. Nevertheless, the variation does not significantly deviate from the black lines in Figure 4, and the black lines can be used as the representative boundaries around the December solstice.

The morphologies of the ion temperature and density at night may reflect nightside ionospheric dynamics as well as vestigial characteristics from the dayside. The observations at 15:00–17:00 LT form a reference for daytime conditions. The morphology of daytime ion temperature is a function of the ion density and SZA. The low ion temperature in the equatorial region is attributed to the high ion density. There is a minor longitude variation in temperature or density in the Northern Hemisphere. Away from the equator, the topside ion temperature is higher in the Southern Hemisphere than in the Northern Hemisphere, except in the American sector where there is a minimum. The temperature variation in the Southern Hemisphere cannot be attributed to the variation in topside ion density, which is similar in the two hemispheres. One possible explanation for the longitudinal variation in the topside ion temperature in the daytime is the longitudinal variation of the magnetic field configuration. In the Southern Hemisphere, the American region corresponds to low magnetic latitudes where the heat conduction from the plasmasphere is not effective.

Because CPE signatures appear in winter, our investigation focuses on the observations in the Northern Hemisphere. By comparing the ion temperature maps at 15:00–17:00 and 20:00–22:00 LT, a region of high temperature is observed at night over North America between 240° and 300°E longitude for 20:00–22:00 LT, which is the expected location based on the conjugate SZA for 20:00–22:00 LT. The high ion temperature near 240°E might be attributed to the anticorrelation between the ion temperature and low ion density there. However, the high ion temperature located near 300°E over North America corresponds to a region of normal or high ion density. The relationship between CPE ion heating and ion density is complicated. CPEs do not produce significant numbers of ions, but they can increase the topside O⁺ density by increasing the scale height. However, since the increased O⁺ scale height causes H⁺ to be pushed to higher altitudes, the total ion density may not be significantly changed at 600 km altitude. FLIP model calculations for December 2003 showed a factor of 2 increase in O⁺ density between the arrival of CPEs and local sunrise, but less than a 50% change in total ion density at 600 km altitude. The patch of higher ion density in the North American sector could be related to the December solstice maximum in plasmasphere density at American longitudes (Richards, Chang, & Comfort, 2000). By 02:00–04:00 LT, the region of high ion temperature and elevated ion density has contracted to between 290° and 320°E, which corresponds with a much narrower region where the conjugate SZA is less than 100°. Higher ionospheric temperatures increase the ion scale height leading to higher topside ion densities.

Figure 5 shows evidence for CPE signatures in the Southern (winter) Hemisphere in the same format as Figure 4 for the June solstice. The black lines are the CPE boundaries calculated for 20:00 and 04:00 LT at the geographic equator on 15 June. In Figure 5a, the ion temperature in the Pacific-American sector (180°–310°E) is higher than that for other longitudes during the daytime, but the ion temperature in this sector is lower than that at other longitudes at night. These day-night and longitudinal variations of the ion temperature are comparable to those of the ion density. In Figure 5b, the ion density in the Pacific-American sector is lower than that at other longitudes during the daytime, but the ion density in this sector is greater than that at other longitudes at night. Therefore, the day-night and longitudinal variation of the ion temperature in the Southern Hemisphere can largely be understood in terms of the anticorrelation between the ion temperature and density.

There is a region with a high ion temperature in the Australian sector (around 120°E) at night that corresponds to the region where CPEs are expected from the sunlit Northern Hemisphere. The variation of its location with LT is consistent with the black SZA curves. An interesting feature in the ion density map at 02:00–04:00 LT is the observation of higher ion density poleward of the black curve around 150°E longitude that is indicated by a black arrow. As a result, a density minimum is formed around 10°S in this region. However, the ion temperature poleward of the black curve is higher than that measured at this density minimum location. This observation provides additional evidence that the high ion temperature in this region is not related to the ion density. Both the high ion temperature and the ion density around 150°E longitude are likely produced by CPEs.

Figure 6 shows the effect of the CPEs on the ion composition through the O⁺ fraction around (a) December solstice and (b) June solstice at 20:00–22:00 and 02:00–04:00 LT. The morphologies of the O⁺ fraction in the winter hemisphere are similar to those of the ion density shown in Figures 4 and 5. The increase in the O⁺ fraction results in the decrease in the light ion (H⁺ and He⁺) fraction. We have investigated the distributions of the O⁺ and H⁺ densities using the ROCSAT-1 observations (not shown). The distribution of the O⁺ density was the same as the ion density. However, the local time behavior of the H⁺ density was not consistent with the O⁺ variations. At 20:00–22:00 LT, the H⁺ density was reduced in the regions heated by CPEs. At 02:00–04:00 LT, the H⁺ density did not show a notable difference compared with that at other longitudes. The behavior of the O⁺ and H⁺ fractions

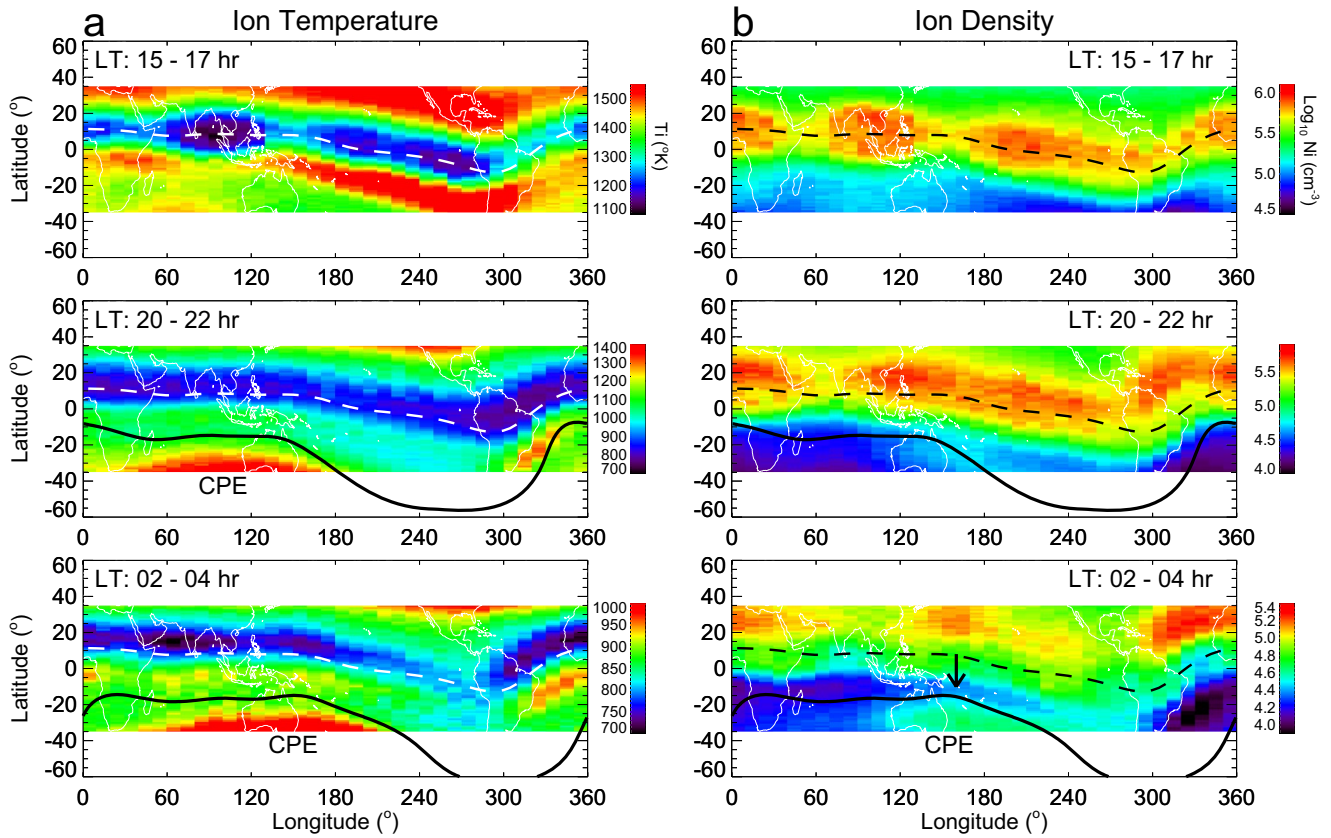


Figure 5. Comparison of the morphologies of the (a) ion temperature and (b) ion density at three LT (15:00–17:00, 20:00–22:00, and 02:00–04:00) around the June solstice (May–August). The locations of conjugate photoelectrons are indicated in the figures. The black arrow at 02:00–04:00 LT in Figure 5b indicates the occurrence of the density minimum at intermediate latitudes.

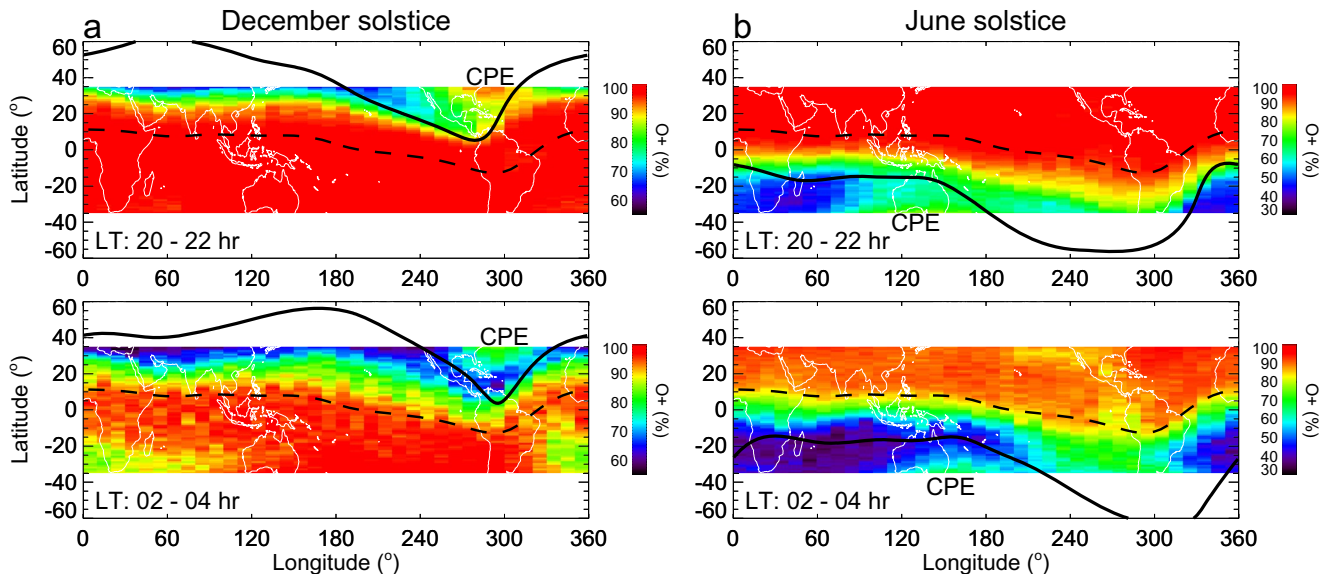


Figure 6. Distributions of the oxygen ion during (a) December and (b) June solstice at 20:00–22:00 and 02:00–04:00 LT. The black curves are the predicted equatorward boundaries of conjugate photoelectrons at 20:00 and 04:00 LTs.

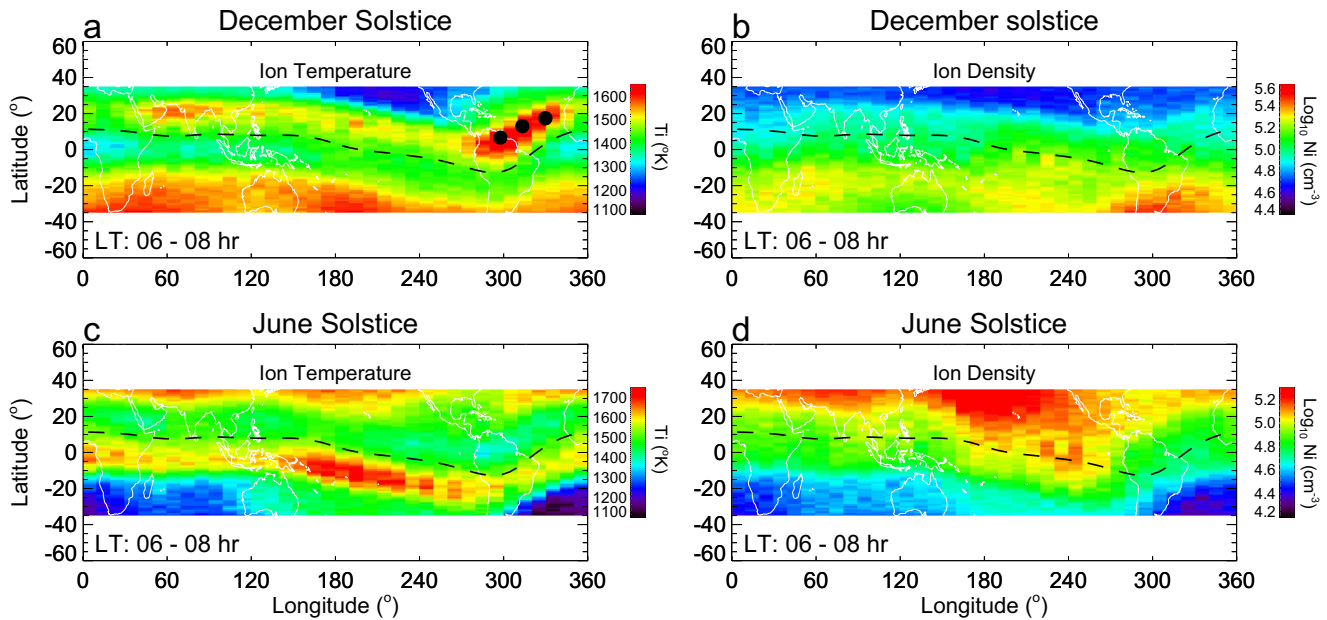


Figure 7. Morphologies of the ion temperature and density early in the morning (06:00–08:00 LT) during (a and b) December solstice and (c and d) June solstice. Black dots in Figure 7a correspond to the locations of the spike-like temperature peaks labeled by “B” in Figure 2a.

and densities at 20:00–22:00 LT can be explained in terms of the oxygen ion scale height. The heating of the topside ionosphere by CPEs increases the O^+ density scale height, resulting in the elevation of the O^+ fraction and density at the satellite altitude. The increase in the O^+ density scale height and its associated ambipolar electric field expels H^+ from the topside into the plasmasphere or reduces the diffusion of H^+ from the plasmasphere, resulting in the decrease in the H^+ fraction and density.

To investigate the spike-like ion temperature enhancement after sunrise, the maps of the ion temperature and density at 06:00–08:00 LT are presented in Figure 7. In the maps of the ion temperature around the December solstice (Figure 7a) and June solstice (Figure 7c), a layer of high ion temperature develops at 10° – 20° N and at 10° – 20° S magnetic latitudes, respectively. Therefore, the spike-like ion temperature enhancement is a winter phenomenon in the ROCSAT data. This phenomenon is most pronounced at 280° – 340° E longitude around December solstices and at 150° – 280° E around June solstices. These locations coincide with the locations of the negative and positive magnetic declinations, respectively. The black dots in Figure 7a correspond to the locations of the temperature peaks indicated by “B” in Figure 2a. The occurrence of the high ion temperature layer in the winter hemisphere can be understood in terms of the combined effects of the low ion density in the winter hemisphere, local photoionization, and a contribution from CPEs. The dependence of the ion temperature on the magnetic declination provides a clue to the CPE contribution to the longitudinal variation of the ion temperature. In the American-Atlantic sector, the sunrise time at the magnetic conjugate point in this longitude region occurs in advance of the local sunrise by 1–2 hr (see A and B peaks in Figure 2). As a result, the CPE heating of the ionosphere at dawn is most significant in the American-Atlantic sector. The situation reverses around June solstices, and the CPE impact on the winter hemisphere is most intense at longitudes where the magnetic declination is positive. This interpretation is consistent with the development of the high ion temperature layer around 200° E longitude in the Southern Hemisphere around June solstices (Figure 7c).

3.3. Conjugate Photoelectron Signatures in Far Ultraviolet Airglow

The thermospheric signatures of CPEs are investigated using the TIMED/GUVI observations of the OI 130.4 nm emission. The maps of OI 130.4 nm emission on four magnetically quiet days are presented in Figure 8: (a) 3 December 2003 (20:00–21:00 LT), (b) 29 December 2003 (03:00–04:00 LT), (c) 4 August 2003 (20:00–21:00 LT), and (d) 30 June 2003 (03:00–04:00 LT). These days are chosen so that the LTs of the airglow observations

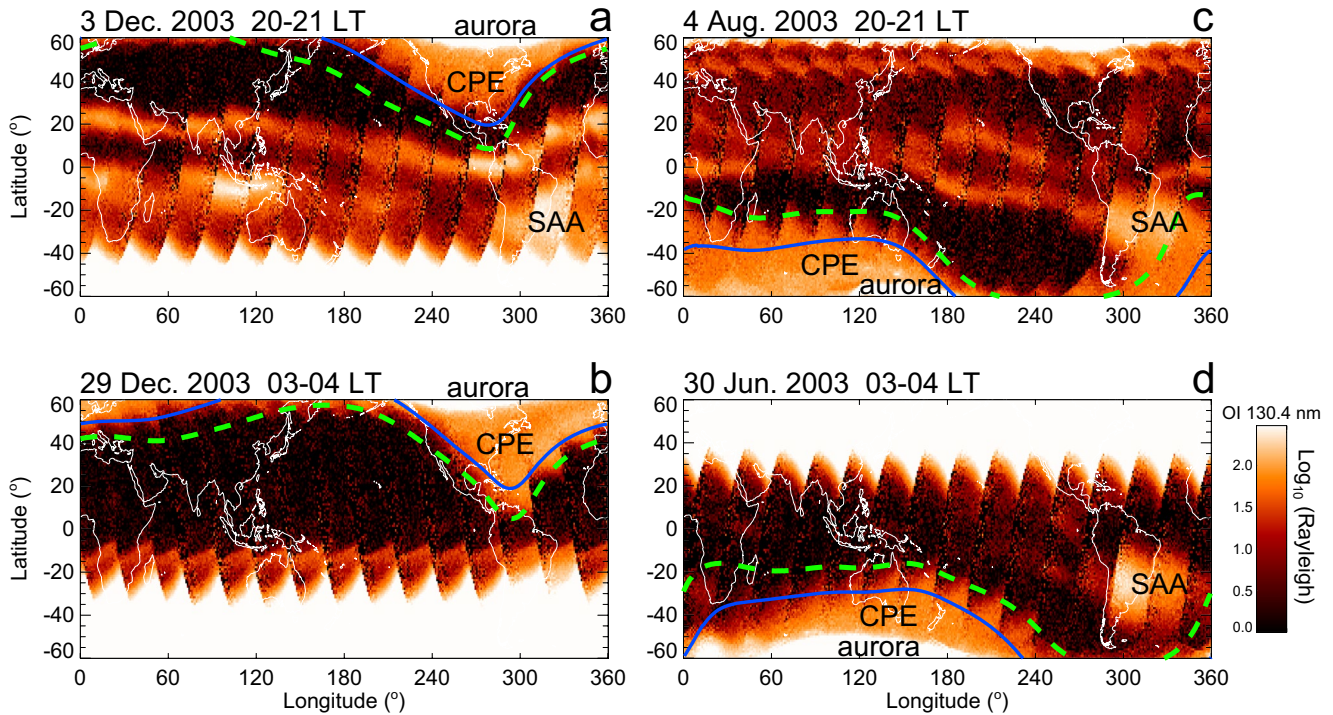


Figure 8. GUVI maps of the OI 130.4 nm emission at (a and b) 20:00–21:00 and 03:00–04:00 LT during the Northern winter and (c and d) 20:00–21:00 and 03:00–04:00 LT during the Southern winter. The green-dashed and blue solid lines in Figures 8a and 8c are the boundaries of conjugate photoelectrons (CPEs) at 20:00 and 21:00 LT, respectively. The green-dashed and blue solid lines in Figures 8b and 8d are the boundaries of CPEs at 04:00 and 03:00 LT, respectively. The locations of CPEs, aurora, and SAA are indicated in the figures.

are close to the LTs of the ionospheric observations shown in Figures 4 and 5. Because of the precession of the TIMED orbit, the observation days at different LT are about 1 month apart in each season. The December observations capture the airglow morphology around the December solstice and the June/August observations capture the airglow morphology around the June solstice. Because the GUVI swath covers about an hour interval, two boundary lines of CPEs are given in each plot. Solid blue lines are for 21:00 and 03:00 LT and dashed green lines are for 20:00 and 04:00 LT. The locations of the CPE and aurora are indicated in the figures. The bright emissions around 320°E and 25°S are associated with the South Atlantic Anomaly (SAA). The good agreement between the morphologies of the airglow and ion temperature (Figures 4 and 5) in the winter hemisphere demonstrates that both phenomena are produced by the same CPE source.

4. Conclusions

Global distributions of the ionospheric and thermosphere signatures of CPEs are investigated using the observations of the ion temperature, density, and composition by the ROCSAT-1 and of the OI 130.4 nm airglow by the TIMED/GUVI. Elevated ion temperature, ion density, oxygen ion density, and oxygen ion fraction are observed at night in the Northern American-Atlantic sector around the December solstice and in the Australian sector around the June solstice. These regions coincide with the locations of the CPE flow from the sunlit hemisphere. The observations of the OI 130.4 nm airglow at the locations of the elevated ion temperatures further support the interpretation of the ionospheric observations. The heating of the ionosphere increases the topside oxygen ion density scale height, which raises the ion density and oxygen ion fraction at the ROCSAT-1 altitude. The CPE signatures in the ion density are less pronounced than those in the ion temperature because the plasma distribution at night is affected by neutral winds and composition. In addition to the enhancements in the ion temperature and density, CPEs can be the source of other ionospheric phenomena. The global morphologies of CPEs in this study provide a useful reference for the identification of ionospheric and thermospheric phenomena associated with CPEs.

Data Availability Statement

ROCSAT-1 data are available from NASA heliophysics Data Portal (<https://spdf.gsfc.nasa.gov/pub/data/formosat-rocsat/formosat-1/pei/>). TIMED/GUVI data are available from <http://guvitimed.jhuapl.edu/>.

Acknowledgments

The work at JHU/APL was supported by the NASA Heliophysics Guest Investigator program NNH19ZDA001N and the U.S. Air Force MURI FA9559-16-1-0364. The FLIP model calculations were provided by Dr. Phil Richards.

References

- Bennett, R. T. (1969). Latitude dependence of 6300 Å (OI) twilight airglow enhancement. *Journal of Geophysical Research*, *74*(1), 381–383. <https://doi.org/10.1029/JA074i001p00381>
- Buckley, J. L., & Moos, H. W. (1971). Vacuum ultraviolet spectra of the late twilight airglow. *Journal of Geophysical Research*, *76*(34), 8378–8383. <https://doi.org/10.1029/JA076i034p08378>
- Burns, A. G., Solomon, S. C., Wang, W., Jee, G., Lin, C. H., Rocken, C., & Kuo, Y. H. (2011). The summer evening anomaly and conjugate effects. *Journal of Geophysical Research*, *116*(A1), A01311. <https://doi.org/10.1029/2010JA015648>
- Burns, A. G., Zeng, Z., Wang, W., Lei, J., Solomon, S. C., Richmond, A. D., et al. (2008). Behavior of the F_2 peak ionosphere over the South Pacific at dusk during quiet summer condition from COSMIC data. *Journal of Geophysical Research*, *113*(A12), A12305. <https://doi.org/10.1029/2008JA013308>
- Carlson, H. C. (1966). Ionospheric heating by magnetic conjugate-point photoelectrons. *Journal of Geophysical Research*, *71*(1), 195–199. <https://doi.org/10.1029/JZ071i001p00195>
- Carlson, R. W., & Suzuki, K. (1974). Observation of O^+ ($^2P_o - ^2D_o$) λ 7319 Å emission in the twilight and night airglow. *Nature*, *248*(5447), 400–401.
- Chao, C. K., Su, S.-Y., & Yeh, H. C. (2003). Presunrise ion temperature enhancement observed at 600 km low and mid-latitude ionosphere. *Geophysical Research Letters*, *30*(4), 1187. <https://doi.org/10.1029/2002GL016268>
- Chen, C. H., Huba, J. D., Saito, A., Lin, C. H., & Liu, J. Y. (2011). Theoretical study of the ionospheric Weddell Sea Anomaly using SAMI2. *Journal of Geophysical Research*, *116*(A4), A04305. <https://doi.org/10.1029/2010JA015573>
- Chen, Y., Liu, L., Le, H., Wan, W., & Zhang, H. (2016). The global distribution of the dusk-to-nighttime enhancement of summer $N_m F_2$ at solar minimum. *Journal of Geophysical Research*, *121*(8), 7914–7922. <https://doi.org/10.1002/2016JA022670>
- Christensen, A. B. (1975). Observations of OI 7774 emission excited by CPEs. *Planetary and Space Science*, *23*(5), 831–842. [https://doi.org/10.1016/0032-0633\(75\)90020-3](https://doi.org/10.1016/0032-0633(75)90020-3)
- Christensen, A. B., Paxton, L. J., Avery, S., Craven, J., Crowley, G., Humm, D. C., et al. (2003). Initial observations with the Global Ultraviolet Imager (GUVI) in the NASA TIMED satellite mission. *Journal of Geophysical Research*, *108*(A12), 1451. <https://doi.org/10.1029/2003JA009918>
- England, S. L., Maus, S., Immel, T. J., & Mende, S. B. (2006). Longitudinal variation of the E-region electric fields caused by atmospheric tides. *Geophysical Research Letters*, *33*(21), L21105. <https://doi.org/10.1029/2006GL027465>
- Evans, J. V. (1965). Cause of the midlatitude evening increase in $f_o F_2$. *Journal of Geophysical Research*, *70*(17), 1175–1185. <https://doi.org/10.1029/JZ070i017p04331>
- Evans, J. V. (1967). Midlatitude electron and ion temperatures at sunspot minimum. *Planetary and Space Science*, *15*(10), 1557–1570. [https://doi.org/10.1016/0032-0633\(67\)90089-X](https://doi.org/10.1016/0032-0633(67)90089-X)
- Evans, J. V. (1973). Seasonal and sunspot cycle variations of F region electron temperatures and protonospheric heat fluxes. *Journal of Geophysical Research*, *78*(13), 2344–2349. <https://doi.org/10.1029/JA078i013p02344>
- Evans, J. V., & Gastman, I. J. (1970). Detection of CPEs at Millstone Hill. *Journal of Geophysical Research*, *75*(2), 807–815. <https://doi.org/10.1029/JA075i004p00807>
- Farley, D. F., McClure, J. P., Sterling, D. L., & Green, J. L. (1967). Temperature and composition of the equatorial ionosphere. *Journal of Geophysical Research*, *72*(23), 5837–5851. <https://doi.org/10.1029/JA072i023p05837>
- Hanson, W. B. (1963). Electron temperatures in the upper atmosphere. *Space Research*, *5*, 282–302.
- He, M., Liu, L., Wan, W., Ning, B., Zhao, B., Wen, J., et al. (2009). A study of the Weddell Sea anomaly observed by FORMOSAT-3/COSMIC. *Journal of Geophysical Research*, *114*(A12), A12309. <https://doi.org/10.1029/2009JA014175>
- Horvath, I. (2006). A total electron content space weather study of the nighttime Weddell Sea Anomaly of 1996/1997 southern summer with TOPEX/Poseidon radar altimetry. *Journal of Geophysical Research*, *111*(A12), A12317. <https://doi.org/10.1029/2006JA011679>
- Horvath, I., & Essex, E. A. (2003). The Weddell Sea Anomaly observed with the TOPEX satellite data. *Journal of Atmospheric and Solar-Terrestrial Physics*, *65*(6), 693–706. [https://doi.org/10.1016/S1364-6826\(03\)00083-X](https://doi.org/10.1016/S1364-6826(03)00083-X)
- Immel, T. J., Sagawa, E., England, S. L., Henderson, S. B., Hagan, M. E., Mende, S. B., et al. (2006). Control of equatorial ionospheric morphology by atmospheric tides. *Geophysical Research Letters*, *33*(15), L15108. <https://doi.org/10.1029/2006GL026161>
- Jee, G., Burns, A. G., Kim, Y.-H., & Wang, W. (2009). Seasonal and solar activity variations of the Weddell Sea Anomaly observed in the TOPEX total electron content measurements. *Journal of Geophysical Research*, *114*(A4), A04307. <https://doi.org/10.1029/2008JA013801>
- Kakinami, Y., Balan, N., Liu, J. Y., & Oyama, K.-I. (2010). Predawn ionospheric heating observed by Hinotori satellite. *Journal of Geophysical Research*, *115*(A1), A01304. <https://doi.org/10.1029/2009JA014334>
- Kakinami, Y., Watanabe, S., Yamamoto, M. Y., & Chao, C.-K. (2014). Correlations between ion density and temperature in the topside ionosphere measured by ROCSAT-1. *Journal of Geophysical Research*, *119*(11), 9207–9215. <https://doi.org/10.1002/2014JA020302>
- Kil, H., DeMajistre, R., Paxton, L. J., & Zhang, Y. (2006). Nighttime F-region morphology in the low and middle latitudes seen from DMSP F15 and TIMED/GUVI. *Journal of Atmospheric and Solar-Terrestrial Physics*, *68*(14), 1672–1681. <https://doi.org/10.1016/j.jastp.2006.05.024>
- Kil, H., Oh, S.-J., Kelley, M. C., Paxton, L. J., England, S. L., Talaat, E. R., et al. (2007). Longitudinal structure of the vertical ExB drift and ion density seen from ROCSAT-1. *Geophysical Research Letters*, *34*(14), L14110. <https://doi.org/10.1029/2007GL030018>
- Kil, H., & Paxton, L. J. (2011). Causal link of longitudinal plasma density structure to vertical plasma drift and atmospheric tides – A review. In M. A. Abdu & D. Pancheva (Eds.), *AGA Special Sopron Book Series: Aeronomy of the Earth's Atmosphere and Ionosphere* (Vol. 2, pp. 349–361). Springer Dordrecht Heidelberg London.
- Kil, H., Schaefer, R. K., Paxton, L. J., & Jee, G.-W. (2020). The far ultraviolet signatures of CPEs seen by the Special Sensor Ultraviolet Spectrographic Imager. *Geophysical Research Letters*, *47*(1), e2019GL086383. <https://doi.org/10.1029/2019GL086383>
- Kil, H., Talaat, E. R., Oh, S.-J., Paxton, L. J., England, S. L., & Su, S.-Y. (2008). The wave structures of the plasma density and vertical ExB drift in low-latitude F region. *Journal of Geophysical Research*, *113*(A9), A09312. <https://doi.org/10.1029/2008JA013106>

- Klimenko, M. V., Klimenko, V. V., Karpachev, A. T., Ratovsky, K., & Stepanov, A. (2015). Spatial features of Weddell Sea and Yakutsk anomalies in f_oF_2 diurnal variations during high solar activity periods: Interkosmos-19 satellite and ground-based ionosonde observations, IRI reproduction and GSM TIP model simulation. *Advances in Space Research*, 55(8), 2020–2032. <https://doi.org/10.1016/j.asr.2014.12.032>
- Lee, W. K., Kil, H., & Paxton, L. J. (2018). Tropical ionization trough seen by Swarm-A satellite. *Geophysical Research Letters*, 45(22), 12135–12141. <https://doi.org/10.1029/2018GL080286>
- Lin, C. H., Liu, C. H., Liu, J. Y., Chen, C. H., Burns, A. G., & Wang, W. (2010). Midlatitude summer nighttime anomaly of the ionospheric electron density observed by FORMOSAT-3/COSMIC. *Journal of Geophysical Research*, 115(A3), A03308. <https://doi.org/10.1029/2009JA014084>
- Lin, C. H., Liu, J. Y., Cheng, C. Z., Chen, C. H., Liu, C. H., Wang, W., et al. (2009). Three-dimensional ionospheric electron density structure of the Weddell Sea Anomaly. *Journal of Geophysical Research*, 114(A2), A02312. <https://doi.org/10.1029/2008JA013455>
- Lin, C. H., Wang, H. W., Hagan, M. E., Hsiao, C. C., Immel, T. J., Hsu, M. L., et al. (2007). Plausible effect of atmospheric tides on the equatorial ionosphere observed by the FORMOSAT-3/COSMIC: Three-dimensional electron density structures. *Geophysical Research Letters*, 34(11), L11112. <https://doi.org/10.1029/2007GL029265>
- Liu, L., Le, H., Chen, Y., He, M., Wan, W., & Yue, X. (2011). Features of the middle- and low-latitude ionosphere during solar minimum as revealed from COSMIC radio occultation measurements. *Journal of Geophysical Research*, 116(A9), A09307. <https://doi.org/10.1029/2011JA016691>
- Lomidze, L., Scherliess, L., & Schunk, R. W. (2016). Modeling and analysis of ionospheric evening anomalies with a physics-based data assimilation model. *Journal of Atmospheric and Solar-Terrestrial Physics*, 140, 65–78. <https://doi.org/10.1016/j.jastp.2016.02.009>
- Meier, R. R. (1971). Observations of conjugate excitation of the OI 1304-Å airglow. *Journal of Geophysical Research*, 76(1), 242–247. <https://doi.org/10.1029/JA076i001p00242>
- Mikhailov, A. V., & Förster, M. (1999). Some F2-layer effects during the January 06–11, 1997 CEDAR storm period as observed with the Millstone Hill incoherent scatter facility. *Journal of Atmospheric and Solar-Terrestrial Physics*, 61(3–4), 249–261. [https://doi.org/10.1016/S1364-6826\(98\)00129-1](https://doi.org/10.1016/S1364-6826(98)00129-1)
- Mikhailov, A. V., Förster, M., & Leschinskaya, T. Y. (2000). On the mechanism of the post-midnight winter N_mF_2 enhancements: Dependence on solar activity. *Annales Geophysicae*, 18(11), 1422–1434. <https://doi.org/10.1007/s00585-000-1422-y>
- Nagy, A. F., & Banks, P. M. (1970). Photoelectron fluxes in the ionosphere. *Journal of Geophysical Research*, 75(31), 6260–6270. <https://doi.org/10.1029/JA075i031p06260>
- Otsuka, Y., Kawamura, S., Balan, N., Fukao, S., & Bailey, G. J. (1998). Plasma temperature variations in the ionosphere over the middle and upper atmosphere radar. *Journal of Geophysical Research*, 103(A9), 20705–20713. <https://doi.org/10.1029/98JA01748>
- Oyama, K.-I., Balan, N., Watanabe, S., Takahashi, T., Isoda, F., Bailey, G. J., & Oya, H. (1996). Morning overshoot of Te enhanced by downward plasma drift in the equatorial topside ionosphere. *Journal of Geomagnetism and Geoelectricity*, 48(7), 959–966. <https://doi.org/10.5636/jgg.48.959>
- Pavlov, A. V., & Pavlova, N. M. (2005). Mechanism of the post-midnight winter night-time enhancements in N_mF_2 over Millstone Hill during 14–17 January 1986. *Journal of Atmospheric and Solar-Terrestrial Physics*, 67(4), 381–395. <https://doi.org/10.1016/j.jastp.2004.11.004>
- Paxton, L. J., Christensen, A. B., Humm, D. C., Ogorzalek, B. S., Pardoe, C. T., Morrison, D., et al. (1999). Global ultraviolet imager (GUVI): Measuring composition and energy inputs for the NASA Thermosphere Ionosphere Mesosphere Energetics and Dynamics (TIMED) mission. In *SPIE Optical Spectroscopic Techniques and Instrumentation for Atmospheric and Space Research III* (Vol. 3756, pp. 265–276). International Society for Optics and Photonics. <https://doi.org/10.1117/12.366380>
- Paxton, L. J., Christensen, A. B., Morrison, D., Wolven, B., Kil, H., Zhang, Y., et al. (2004). GUVI: A hyperspectral imager for geospace. In C. A. Nardell, P. G. Lucey, J. H. Yee, & J. B. Garvin (Eds.), *Instruments, Science, and Methods for Geospace and Planetary Remote Sensing, Proceedings of SPIE - The International Society for Optical Engineering* (Vol. 5660, pp. 227–240). <https://doi.org/10.1117/12.579171>
- Paxton, L. J., Meng, C.-I., Fountain, G. H., Ogorzalek, B. S., Darlington, E. H., Goldsten, J., et al. (1993). SSUSI: Horizon-to-horizon and limb-viewing spectrographic imager for remote sensing of environmental parameters. In *Ultraviolet technology IV, SPIE*, (Vol. 1764, pp. 161–176). International Society for Optics and Photonics. <https://doi.org/10.1117/12.140846>
- Paxton, L. J., Schaefer, R. K., Zhang, Y., & Kil, H. (2017). Far ultraviolet instrument technology. *Journal of Geophysical Research: Space Physics*, 122(2), 2706–2733. <https://doi.org/10.1002/2016JA023578>
- Paxton, L. J., Zhang, Y., Kil, H., & Schaefer, R. K. (2021). Exploring the upper atmosphere: Using optical remote sensing. *Upper Atmosphere Dynamics and Energetics*, 487–522. <https://doi.org/10.1002/9781119815631.ch23>
- Richards, P. G., Buonsanto, M. J., Reinisch, B. W., Holt, J., Fennelly, J. A., Scali, J. L., et al. (2000). On the relative importance of convection and temperature to the behavior of the ionosphere in North America during January 6–12, 1997. *Journal of Geophysical Research*, 105(A6), 12763–12776. <https://doi.org/10.1029/1999JA000253>
- Richards, P. G., Chang, T., & Comfort, R. H. (2000). On the causes of the annual variation in the plasmaspheric electron density. *Journal of Atmospheric and Solar-Terrestrial Physics*, 62(10), 935–946. [https://doi.org/10.1016/S1364-6826\(00\)00039-0](https://doi.org/10.1016/S1364-6826(00)00039-0)
- Richards, P. G., Dyson, P. L., Davies, T. P., Parkinson, M. L., & Reeves, A. J. (1998). Behavior of the ionosphere and thermosphere at a southern midlatitudes station during magnetic storms in early March 1995. *Journal of Geophysical Research*, 103(26), 26421–26432. <https://doi.org/10.1029/97JA03342>
- Richards, P. G., Meier, R. R., Chen, S., & Dandenault, P. (2018). Investigation of the causes of the longitudinal and solar cycle variation of the electron density in the Bering Sea and Weddell Sea anomalies. *Journal of Geophysical Research: Space Physics*, 123(9), 7825–7842. <https://doi.org/10.1029/2018JA025413>
- Richards, P. G., Meier, R. R., Chen, S.-P., Drob, D. P., & Dandenault, P. (2017). Investigation of the causes of the longitudinal variation of the electron density in the Weddell Sea Anomaly. *Journal of Geophysical Research*, 122(6), 6562–6583. <https://doi.org/10.1002/2016JA023565>
- Richards, P. G., & Peterson, W. K. (2008). Measured and modeled backscatter of ionospheric photoelectron fluxes. *Journal of Geophysical Research*, 113(A8), A08321. <https://doi.org/10.1029/2008JA013092>
- Richards, P. G., & Wilkinson, P. J. (1998). The ionosphere and thermosphere at southern midlatitudes during the November 1993 ionospheric storm: A comparison of measurement and modeling. *Journal of Geophysical Research*, 103(A5), 9373–9389. <https://doi.org/10.1029/98JA00289>
- Sagawa, E., Immel, T. J., Frey, H. U., & Mende, S. B. (2005). Longitudinal structure of the equatorial anomaly in the nighttime ionosphere observed by IMAGE/FUV. *Journal of Geophysical Research*, 110(A11), A11302. <https://doi.org/10.1029/2004JA010848>
- Savitzky, A., & Golay, M. J. E. (1964). Smoothing and differentiation of data by simplified least squares procedures. *Analytical Chemistry*, 36(8), 1627–1639. <https://doi.org/10.1021/ac60214a047>
- Scherliess, L., Thompson, D. C., & Schunk, R. W. (2008). Longitudinal variability of low-latitude total electron content: Tidal influences. *Journal of Geophysical Research*, 113(A1), A01311. <https://doi.org/10.1029/2007JA012480>
- Schunk, R. W., & Nagy, A. F. (1978). Electron temperatures in the F region of the ionosphere: Theory and observations. *Reviews of Geophysics*, 16(3), 355–399. <https://doi.org/10.1029/RG016i003p00355>

- Shepherd, G. G., Cho, Y.-M., Fomichev, V. I., & Martynenko, O. V. (2014). Characteristics of the O⁺(²P–²D) 732.0 and 733.0 nm airglow emissions observed with WINDII and simulated with the C-IAM. *Geophysical Research Letters*, *41*(15), 5354–5360. <https://doi.org/10.1002/2014GL060840>
- Solomon, S. C., Andersson, L., Burns, A. G., Eastes, R. W., Martinis, C., McClintock, W. E., & Richmond, A. D. (2020). Global-scale observations and modeling of far-ultraviolet airglow during twilight. *Journal of Geophysical Research: Space Physics*, *125*(3), e2019JA027645. <https://doi.org/10.1029/2019JA027645>
- Stolle, C., Liu, H., Truhlik, V., Lühr, H., & Richards, P. G. (2011). Solar flux variation of the electron temperature morning overshoot in the equatorial F region. *Journal of Geophysical Research*, *116*(A4), A04308. <https://doi.org/10.1029/2010JA016235>
- Strickland, D. J., & Anderson, D. E., Jr. (1977). The OI 1304-Å nadir intensity/column production rate ratio and its application to airglow studies. *Journal of Geophysical Research*, *82*(7), 1013–1016. <https://doi.org/10.1029/ja082i007p01013>
- Su, S.-Y., Yeh, H. C., & Heelis, R. A. (2001). ROCSAT 1 ionospheric plasma and electrodynamics instrument observations of equatorial spread F: An early transitional scale result. *Journal of Geophysical Research*, *106*, 29153–29159. <https://doi.org/10.1029/2001JA900109>
- Sultan, P. J., & Rich, F. J. (2001). Determination of a proxy for F region meridional neutral winds using in situ satellite ion density measurements. *Journal of Geophysical Research*, *106*(A10), 21033–21038. <https://doi.org/10.1029/2000JA000219>
- Urco, J. M., Kamalabadi, F., Kamaci, U., Harding, B. J., Frey, H. U., Mende, S. B., et al. (2021). Conjugate photoelectron energy spectra derived from coincident FUV and radio measurements. *Geophysical Research Letters*, *48*(23). <https://doi.org/10.1029/2021GL095839>
- West, K. H., & Heelis, R. A. (1996). Longitude variations in ion composition in the morning and evening topside equatorial ionosphere near solar minimum. *Journal of Geophysical Research*, *101*(A4), 7951–7960. <https://doi.org/10.1029/95JA03377>
- West, K. H., Heelis, R. A., & Rich, F. J. (1997). Solar activity variations in the composition of the low-latitude topside ionosphere. *Journal of Geophysical Research*, *102*(A1), 295–305. <https://doi.org/10.1029/96JA03031>
- Yang, T.-Y., Park, J., Kwak, Y.-S., Oyama, K.-I., Minow, J. I., & Lee, J.-J. (2020). Morning overshoot of electron temperature as observed by the Swarm constellation and the International Space Station. *Journal of Geophysical Research: Space Physics*, *125*(2), e2019JA027299. <https://doi.org/10.1029/2019JA027299>
- Zhang, Y., Paxton, L. J., & Schaefer, R. K. (2021). Ionospheric and thermospheric contributions in TIMED/GUVI O 135.6 nm radiances. *Geophysical Research: Space Physics*, *126*(9), e2021JA029333. <https://doi.org/10.1029/2021JA029333>